Characterization of Retinal Arteries by Adaptive Optics Ophthalmoscopy Image Analysis

F Rossant Rossant, Isabelle Bloch, I. Trimèche, J.-B. de Regnault de Bellescize, D. Castro Farias, V. Krivosic, H. Chabriat, M. Paques

To cite this version:

F Rossant Rossant, Isabelle Bloch, I. Trimèche, J.-B. de Regnault de Bellescize, D. Castro Farias, et al.. Characterization of Retinal Arteries by Adaptive Optics Ophthalmoscopy Image Analysis. IEEE Transactions on Biomedical Engineering, 2024, 71 (11), pp.3085-3097. ⟨10.1109/TBME.2024.3408232⟩. ⟨hal-05362555⟩

Characterization of Retinal Arteries by Adaptive Optics Ophthalmoscopy Image Analysis

F. Rossant, I. Bloch, I. Trimèche, J.-B. de Regnault de Bellescize, D. Castro Farias, V. Krivosic, H. Chabriat, and M. Paques

***Abstract*—*Objective:* This paper aims at quantifying biomarkers from the segmentation of retinal arteries in adaptive optics ophthalmoscopy images (AOO). *Methods:* The segmentation is based on the combination of deep learning and knowledge-driven deformable models to achieve a precise segmentation of the vessel walls, with a specific attention to bifurcations. Biomarkers (junction coefficient, branching coefficient, wall to lumen ratio (wlr)) are derived from the resulting segmentation. *Results:* reliable and accurate segmentations ($mse = 1.75 \pm 1.24$ pixel) and measurements are obtained, with high reproducibility with respect to images acquisition and users, and without bias. *Significance:* In a preliminary clinical study of patients with a genetic small vessel disease, some of them with vascular risk factors, an increased wlr was found in comparison to a control population. *Conclusion:* The wlr estimated in AOO images with our method (AOV, Adaptive Optics Vessel analysis) seems to be a very robust biomarker as long as the wall is well contrasted.**

***Index Terms*—Adaptive optics ophthalmoscopy, retina vessel walls segmentation, biomarkers, deep learning, deformable models.**

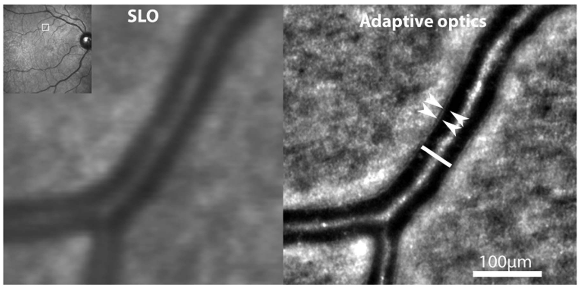

Fig. 1. Conventional SLO (left) and AOO (right) of a normal artery, AOO showing improved details of the vessel (bar: lumen; arrowheads bracket: wall).

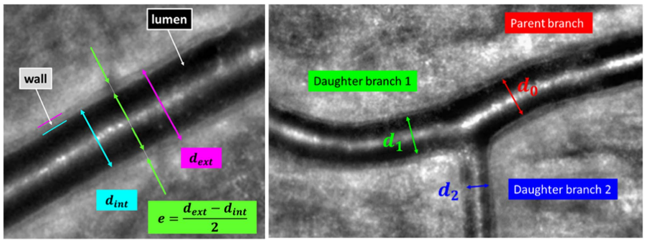

(a) (b)

Fig. 2. AOO images of retinal arteries and diameters involved in the estimation of biomarkers; (a) artery branch with well contrasted walls; (b) arterial bifurcation.

I. INTRODUCTION

DISEASES such as diabetes and high blood pressure are growing in incidence, generating new needs for microvascular diagnosis. The retina, easily accessible by imaging, offers an observation window of the human microvascular network, giving a unique opportunity for deciphering the anatomy and physiology of human microvessels. It has been already shown that non-ophthalmic pathologies can be predicted by analyzing changes in the retinal vasculature: numerous systemic diseases such as cardiovascular hypertension [1], [2], diabetes [3], [4], ischemic heart disease and stroke [5] have reported alterations in retinal arteries and veins. This underlines the importance of phenotyping of retinal microvessels thanks to eye fundus imaging.

In clinical routine, confocal scanning laser ophthalmoscopy (cSLO) (Fig. 1, left) or optical coherence tomography angiography (OCTA) are the common imaging modalities used to detect retinal vascular abnormalities. However, the diagnosis is most often based on non-quantitative scales. Moreover, the resolution of these images is not sufficient to quantify subtle morphometric changes or to analyze micrometric structures such as the arterial wall. Nowadays, adaptive optics ophthalmoscopy (AOO, Fig. 2, right) offers a much higher image resolution (about 1 to 2 μm/pixel against 10 to 20 μm/pixel) paving the way to quantitative monitoring of microvascular effects of diseases [6].

In the literature, several morphometric parameters have been explored to characterize arterial branches and bifurcations, and

---

Manuscript received 15 May 2023; revised 26 January 2024; accepted 20 May 2024. Date of publication 3 June 2024; date of current version 22 October 2024. This work was supported by the French Agence Nationale de la Recherche under Grant ANR-16-RHUS-0004 (RHU TRT-cSVD). *(Corresponding author: F. Rossant.)*

F. Rossant is with the Institut Supérieur d'Electronique de Paris, Isep, 92130 Issy-les-Moulineaux, France (e-mail: florence.rossant@isep.fr).

I. Bloch is with the Sorbonne Université, CNRS, LIP6, France, and also with LTCI, Télécom Paris, Institut Polytechnique de Paris, France.

I. Trimèche was with the Institut Supérieur d'Electronique de Paris, Isep, France. He is now with Braintale, France.

J.-B. de Regnault de Bellescize was with the Institut Supérieur d'Electronique de Paris, Isep, France. He is now with Euranova, Belgium.

D. Castro Farias and M. Paques are with the Clinical Investigation Center 1423 of the Centre Hospitalier National d'Ophtalmologie des Quinze-Vingts, France.

V. Krivosic and H. Chabriat are with the Referral Centre CERVCO at the University Hospital Lariboisière in APHP (University Paris Cité), France.

Digital Object Identifier 10.1109/TBME.2024.3408232

correlate biomarkers to pathologies [7]. Thickening of the arterial wall may result from hypertension [1]. Coefficients derived from diameter measurements at an arterial bifurcation (e.g., junction exponent, branching coefficient) may reveal vascular remodeling in diabetes [3] and, in general, inappropriate blood flow distribution [8]. Interpretating and monitoring these measurements require high-resolution imaging, thus AOO, as well as robust and accurate segmentation algorithms to estimate diameters.

However, there is a lack of software tools to automatically segment vessels in AOO images and compute derived biomarkers. In [9], the segmentation of the arterial wall is based on a spline interpolation from manually defined control points. Therefore, most clinical studies in AOO do not rely on image segmentation, but on manual [3] or semi-automatic measurements of local features, mainly diameters and parietal thickness. In [10], the vessel width is measured at five parallel cross-sections, the position of the central one being manually defined. Of the three proposed algorithms, the sliding linear regression filter (SLRF) is selected as the most accurate approach for identifying vessel edges and deriving diameter [11]. Local analysis of the pixel intensities at a particular cross-section is also used in [12], [13], [14] thanks to the semi-automated software proposed by Imagine Eyes [15]. While manual methods do not guarantee accuracy or reproducibility of biomarkers, semi-automated methods are more robust but time consuming and subject to variability due to manual selection of the measurement location. So, there is a real need of fully automatic segmentation methods to systematize the estimation of biomarkers on relevant and automatically defined regions. Such an algorithm could also pave the way to a more global analysis of the vascular tree. However, segmenting automatically AOO images is very challenging. The main difficulties are related to the great variability of these images, the high textured background, local blur due to local defocus (typically at arterio-venous crossings), and the poor contrast of the parietal wall.

In this article, we propose a complete framework, AOV, to segment vessels in flood-illumination AOO (the only commercially available AOO system [16]) and compute biomarkers characterizing arteries and arterial bifurcations.

The remainder of the article is organized as follows. In Section II, we introduce the main biomarkers we want to calculate from the images and we describe briefly our database and the targeted clinical application. Section III is dedicated to image segmentation, as an extension of our previous work [17], [18], [19], relying on a convolutional neural network and active contour models. Given the difficulty to segment the arteries with the required accuracy, we propose several usage modes, from the completely automatic one to semi-automatic ones, where the user basically initializes or reinitializes manually the deformable models to focus on a specific area or to achieve a better segmentation. Compared to our previous work [17], [18], [19], the novelty is threefold: (i) we present a complete framework to process AOO images with or without supervision; (ii) we have extended our active contour model to introduce more coupling between the interfaces to be detected, and (iii) we introduce an optimized strategy in the parameter setting. All this allowed us to obtain better performances in terms of robustness, precision, reproducibility, and, at the end, to propose the first operational software for clinical studies. In Section IV, we present a theoretical and experimental study to quantify the sensitivity of the biomarkers to segmentation imprecision, an analysis which has never been done before. Section V summarizes our experiments to evaluate the proposed methods in the several usage modes, in terms of reproducibility, robustness and accuracy. All results of Sections IV and V enable us to select relevant biomarkers and define objectively which minimal vessel caliber is required to get reliable measurements for clinical applications. Finally, we discuss preliminary medical results obtained on images of control subjects and patients with CADASIL (Cerebral Autosomal Dominant Arteriopathy with Subcortical Infarcts and Leukoencephalopathy), a systemic small vessel disease of genetic origin (Section VI), and conclude (Section VII).

II. VASCULAR MORPHOMETRY IN AOO

Our study focuses on the estimation of biomarkers that characterize arterial branches and bifurcations in AOO images. We describe briefly this imaging modality, then we define the morphometric parameters that will be derived from the segmentations and we introduce our database.

A. Adaptive Optics Ophthalmoscopy (AOO)

Vessel imaging was performed with a commercially available adaptive optics system [16]. The rtx1 camera corrects wavefront aberrations with a 750 nm super luminescent diode source and an adaptive optics system operating in a closed loop. This camera uses an infrared flood illumination, with a transverse resolution of 2 microns that enables a high precision imaging of the vessel wall. The final image covers an area of 4°x4°, which results from stacking 40 fundus images for 2 seconds, according to the protocol in [1].

B. Morphometry

AOO (Fig. 2) enables us to see the arteriolar walls and, therefore, to calculate the wall-to-lumen ratio, defined as the ratio between the wall thickness $e = (d_{ext} - d_{int})/2$ to the inner radius $d_{int}/2$, where d_{int} and d_{ext} are the internal and external diameters, respectively:

$$wlr = \frac{e}{d_{int}/2} = \frac{d_{ext} - d_{int}}{d_{int}} \quad (1)$$

The wlr may indicate the degree of vascular tone, that is, contricted vessels show a higher thickness wall and a diminished lumen diameter, and is believed to represent an adaptive mechanism to high blood pressure.

The geometry of the arteriolar arborescence, where in a bifurcation one single branch divides into two different daughter branches, can help us study its energetic efficiency [20]. Based on Murray's law, or the minimal work principle, blood flow should be proportional to the cube of the vessel radii. To preserve this flow, there exists a cubic relationship between the inner diameter of parent (d_0, Fig. 2(b)) and those of daughter vessels (d_1 and d_2): $d_0^3 = d_1^3 + d_2^3$. The junction coefficient is a way of quantifying the conformation of the microvascular network according to Murray's law. It is defined as x solving:

$$d_0^x = d_1^x + d_2^x \tag{2}$$

and its expected value is 3. Nevertheless, solving (2) may lead to negative values of x, which has no physiological interpretation, since we do not consider enlargements of the vessels after the bifurcation. In this case, we will consider that the junction exponent cannot be calculated.

Another biomarker is the branching coefficient β:

$$\beta = \frac{d_1^2 + d_2^2}{d_0^2} = \frac{1+\lambda^2}{(1+\lambda^x)^{\frac{2}{x}}} \tag{3}$$

where λ is the coefficient of asymmetry, defined as:

$$\lambda = \frac{d_2}{d_1} \, \epsilon \,]0, \, 1] \tag{4}$$

Considering an ideal bifurcation with an optimal branching coefficient $x = 3$ (Murray's law), we calculate the deviation β_{dev} to the optimum as

$$\beta_{dev} = \frac{d_1^2 + d_2^2}{d_0^2} - \frac{1+\lambda^2}{(1+\lambda^3)^{\frac{2}{3}}} \tag{5}$$

This biomarker is always calculable and provides information on the deviation to Murray's law optimum: a positive deviation indicates that downstream resistances are lower than optimal, and vice versa. This does not preclude the cause of such variations (e.g., dilation or constriction of upstream or downstream vessel) nor which vessel is the cause.

C. Database

Patients were evaluated during their routine care in the National Referral Centre for Rare Cerebrovascular Diseases in France (CERVCO) from the institution APHP (Assistance Publique des Hôpitaux de Paris). The study was an observational study and was not declared as a trial on clinicaltrials.gov. The study was approved by an independent ethics committee (updated agreement CEEI-IRB-17/388) from INSERM–France and conducted in accordance with the Declaration of Helsinki and guidelines for Good Clinical Practice and General Data Protection Regulation (GDPR) in Europa.

Patients with a good visual fixation and clear optical structures that allowed for a neat visualization of the retina were selected. Pupil dilation was necessary. We determined, as the region of interest, the supero-temporal vessel arcade of the right eye. We followed the largest artery until its temporal localization, and looked to image as many bifurcations as possible, until the vessels walls were no longer discernable.

We included 31 healthy subjects without systemic or ophthalmological diseases and 107 patients with CADASIL, a genetic form of small vessel disease of the brain that can be exacerbated by vascular risk factors such as hypertension [21]. As retinal vessels are related to cerebral vessels, sharing many structural, functional and pathological features, we can assume that the analysis of retinal vessel alterations observable in 2D AOO images will enable us to define relevant biomarkers in a progressive small vessel disease as CADASIL. The database contains 533 images centered on an arterial bifurcation. This database was divided into two parts, having a similar ratio of images from control subjects and CADASIL subjects: sub-database A contains 265 images selected to train and test the convolutional neural network (Section III-C-1)). These images were manually annotated to get the binary mask of the vessel lumen of both arteries and veins. The other 268 images (sub-database B) were used to analyze biomarker behavior with realistic data (Section IV) and for the quantitative evaluation of our algorithms (Section V).

III. AOV FRAMEWORK: USAGES MODALITIES AND SEGMENTATION METHODS

A. State of the Art

Segmentation of blood vessels in various parts of the body and in different image modalities has raised a lot of developments. Methods can be roughly divided into two classes: (1) "structural" methods, that rely on prior information on the vessels and their appearance in the given images, and (2) learning-based methods, where all the information is supposed to be contained in a database of images. The methods of the first type have been extensively described in [22]. A geometrical model of the vessel is defined (usually a generalized cylinder, and specific models for bifurcations), appearance information is extracted from the image (e.g., Hessian-based measures, flow of the gradient), and an extraction scheme is designed, formalized either as a segmentation process (typically using deformable models), or as a tracking process (e.g., using minimal path or particle filters). Learning-based approaches are summarized in [23], including unsupervised (such as automated clustering) or supervised (e.g., support vector machines, random forests, convolutional neural networks), where a reference segmentation has to be provided for each image of the training set.

As for retina vessels, where the segmentation mainly aims at computing biomarkers, especially close to bifurcations, most work focused on standard eye fundus images. Very little was done on AOO images, although their better resolution allows for more accurate estimation of vessel diameters and derived biomarkers. Among the few existing work, a semi-automatic method was proposed in [9] based on a spline interpolation of the vessel walls from manually defined control points. However, the manual steps induce a lack of reproducibility, and the spline approximation a lack of accuracy. A deformable model was proposed in [17] to segment automatically the contours of the vessel walls using an approximate parallelism constraint [24]. This method is robust and accurate for vessel segments, but not for bifurcations. These two approaches are typical examples of methods of the first type. As for the second type of methods, convolutional neural networks (CNN) are more and more developed, in particular with the success of U-Net [25] and nnU-Net [26] for medical image segmentation. Several variants of CNN architectures have been designed for the segmentation of retina vessels in eye fundus images (e.g., [27], [28], [29] with an additional spatial regularization based on conditional random fields, [30] using GAN, [31] and [32] using residual blocks, [33] handling unbalanced classes in the loss function). All these methods should be adapted to be able to process AOO images. They usually do not include prior information (besides the training dataset, and sometimes a regularization as post-processing). They may lack accuracy in some specific cases.

B. AOV Framework and Usage Modalities

In this paper, we propose an original approach, which combines both types of methods, "structural" and "learning-based", taking advantages of each of them and compensating for their drawbacks. Given the difficulty to segment the arteries with the required accuracy, we have developed a framework, AOV, in which the user can keep control on the segmentation task. To this end, we propose to apply parametric contour models as powerful segmentation tools that are easy to initialize manually, if necessary. In the initial model [34], a parametric curve $V(s)$ evolves dynamically through the minimization of a given energy functional to reach the boundary of the object to be segmented. However, this method is sensitive to the initial curve position. To overcome these problems, one can first look for methods that ensure a good initialization (close to the solution) and one can also introduce prior knowledge in the energy functional to better drive the minimization process, as in [24]. That is why we propose 1/ to rely on deep learning to initialize automatically our deformable models, since this approach allows to cope with the high variability of the data in terms of image quality and vessel characteristics, and 2/ new energy functionals embedding structural constraints to make the contour evolution more robust to noise, blur and high gradients in the background. This strategy provides good results in a fully automatic process while allowing the user to easily reinitialize manually the active contour models in case of failure. It is also possible to directly initialize the algorithm manually to focus on a specific region in the image.

Concretely, we have designed a framework with two possible usage modes, either fully automatic or semi-automatic where the user keeps control on the segmentation initialization (Fig. 3). In the fully automatic mode, the segmentation is initialized as a preliminary segmentation mask predicted by a convolutional network, an optimized U-Net designed to be robust to various sizes and orientations of the vessel branches. This initial result is then refined in a second step using advanced parametric models, with specific adaptations to accurately delineate the artery walls and handle bifurcations. In the semi-automatic mode, the only intervention of the user is to manually define the central reflection line of the vessel branches by a few points, the rest of the segmentation being carried out automatically. This manual step is easy to perform, it enables the user to focus on the vessel or bifurcation of interest instead of processing the whole image. It also allows complex configurations of arterio-venous crossings to be processed by explicitly entering the branches to be segmented. A supervision is possible in both modes: the user can reinitialize manually the active contour model if he is not satisfied with the final segmentation. This usage flexibility has proved to be very efficient for processing large databases for medical studies: most interfaces can be accurately segmented in the fully automatic mode, and manual interventions, if needed, are minimized and very easy to carry out. In any case, a good reproducibility of the measurements is ensured, since the last segmentation steps are always automatic (Section V).

C. Proposed Segmentation Methods

As previously explained, the core of our segmentation method is based on a dedicated parametric active contour algorithm embedding structural *a priori* knowledge to achieve better robustness and accuracy, combined with deep-learning to initialize the process. In this sub-section, we focus on the proposed models, summarizing our previous work [17], [18], [19] and emphasizing the improvements. Implementation details are given in the Appendix.

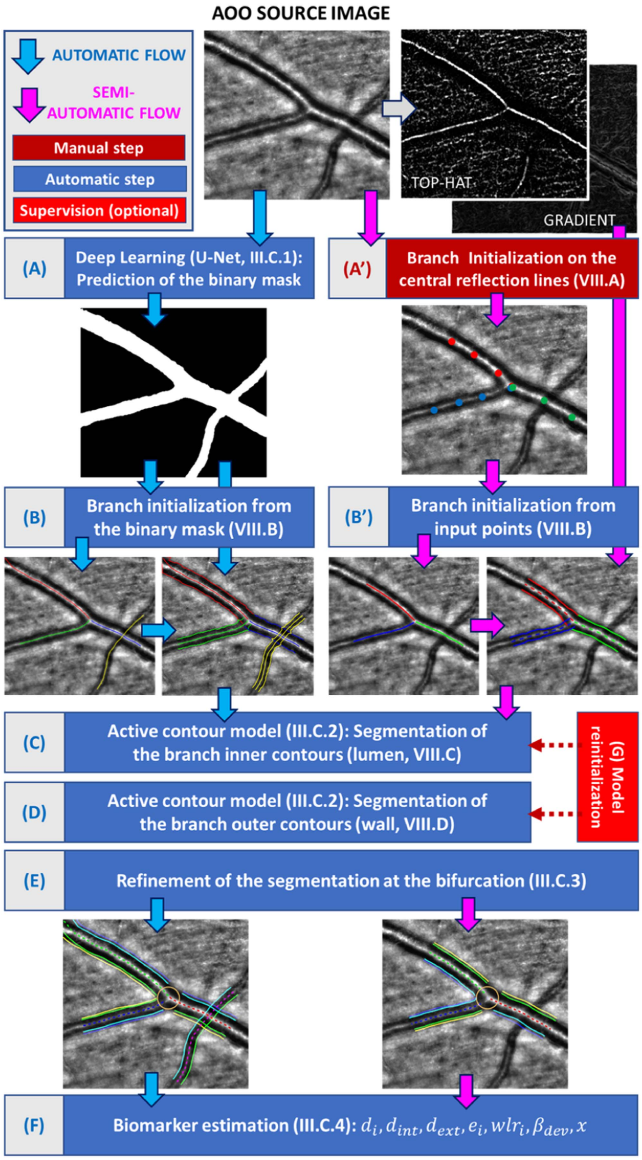

Fig. 3. AOV usage modes. AOV software allows for different levels of interactivity to reach high performances in terms of accuracy and reproducibility of the measurements while minimizing the user's intervention.

1) Extraction of a Binary Mask Based on Deep Learning: We remind here briefly the design of our U-Net [19] to extract the binary mask of the vessel lumen (Fig. 3(A)), the main improvement coming from the extension of our annotated database to better represent the high variability in the images. The popular U-Net [25] was used as a base model. In order to cope with different vessel sizes, even in one same image, we propose to replace the convolution blocks of the original architecture by the feature extractor from the InceptionResNetV2 network [32], [35] (without the last dense layers), which integrates filters of different sizes at every level. In addition, its variety of receptive fields and short-cut connections showed remarkable results in both processing time and performance. Moreover, we have added a *Fire-squeeze* block to the central stage of the U-Net (bottleneck) as suggested in [27]. This block replaces 3 x 3 filters with 1x1 filters (Squeeze layer), decreasing the number of input channels to the next layer. Thus, we integrate a structure that breaks up the characteristics into three convolutional layers each applying a mask of different size (1x1, 3 x 3 and 5 x 5) and then recombines them by a 1 x 1 convolution. This produces larger activation maps which can lead to higher classification accuracy. We refer the reader to [19] for the quantitative evaluation that justifies the final proposed architecture, the residual U-Net [31] being used as baseline model.

The network is trained to optimize the Dice score as loss function. A pre-trained version of the U-net, on ImageNet [36], was used. This allows fine-tuning the network on a limited number of data and in a fast way. To do so, the sub-database A of 265 annotated images was divided as follows: 190 images were selected to train the network, 22 images were selected as the validation set and 53 other images sharing the same characteristics were selected for the testing set. To ensure the capability of our model to segment precisely all types of vessels, we have imposed the following criteria to build our learning dataset: (1) a balanced number of arteries and veins; (2) a balanced number of sharp images and blurred images; (3) presence of arteriovenous crossings; (4) presence of arterial bifurcations and venous confluences; (5) presence of healthy and pathological vessels (diabetic, hypertensive …). Additionally, data augmentation was applied, using spatial transformations and intensity variations, again to cope with the potential variability of vessel orientation and intensity.

Training was performed according to [19], using stochastic gradient descent with an adaptive moment estimator (Adam) [37]. The Dice score obtained on the test set with the proposed architecture is equal to 0.980 and the boundary F1 metric is equal to 0.976. These results are slightly better than the ones presented in [19], thanks to the enlargement of the training set which now represents better the great variability of AOO images. Our experiments also confirm that the proposed combination of U-Net, InceptionResNetV2 and fire-squeeze leads to better performances compared to the standard U-Net; but the benefit of the squeeze layer decreases when the size of the training set increases. Fig. 4 illustrates the obtained results. The segmentation is generally very good, and the model is able to segment large vessels as well as smaller ones with more blur and discontinuities in the central reflection line. The vascular tree is most often well detected, without splitting. However, a few local improvements are still needed, as indicated by the red rectangles in the figures. Moreover, this method provides only a mask of the vessel lumen, it does not distinguish the internal and external vessel walls, and the structure of the vascular tree has to be recovered.

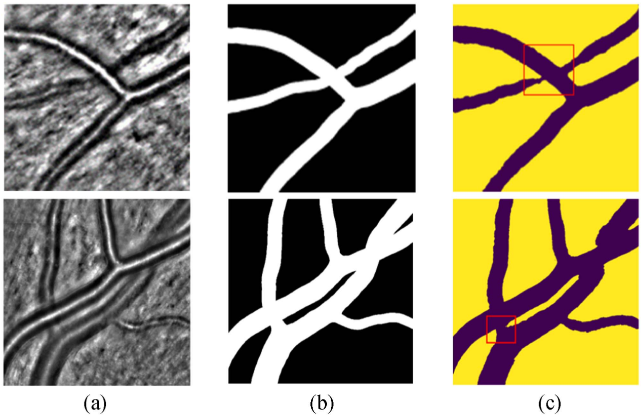
(a) (b) (c)

Fig. 4. Segmentation results. (a) Original AOO images. (b) Corresponding reference segmentations. (c) Vessel masks predicted by the proposed method. The red rectangles indicate where local improvement is needed.

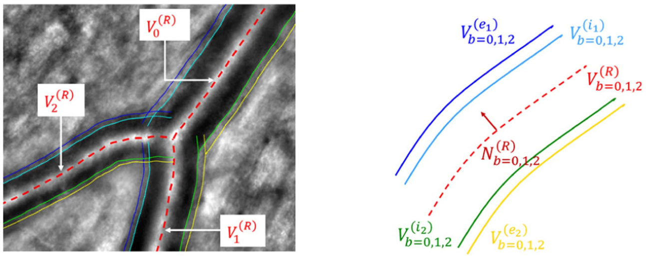

Fig. 5. Branch segmentation model. b denotes the branch index in a bifurcation.

2) Active Contour Model for the Segmentation of the Arterial Branches: The approach is based on coupled active contours, with structural constraints. Fig. 5 presents the geometrical model on which the method relies. Each vessel branch b is represented by five approximately parallel lines, the central reflection line $V_b^{(R)}$, and the inner $V_b^{(i_1,\,2)}$ and outer contours $V_b^{(e_1,\,2)}$ of the vessel wall, on each side of the central line. Each point on a contour is defined as the sum of the corresponding point on the central line and a vector along the normal $N_b^{(R)}$ with norm equal to the half diameter, as expressed by (6):

$$\begin{cases} V_b^{(e_1)} = V_b^{(R)} + b_b^{(e_1)}\ N_b^{(R)} \\ V_b^{(i_1)} = V_b^{(R)} + b_b^{(i_1)}\ N_b^{(R)} \end{cases} \quad \begin{cases} V_b^{i_2} = V_b^{(R)} + b_b^{(i_2)}\ N_b^{(R)} \\ V_b^{(e_2)} = V_b^{(R)} + b_b^{(e_2)}\ N_b^{(R)} \end{cases}$$
$$b_b^{(i_1)},\ b_b^{(e_1)} > 0 \qquad\qquad b_b^{(i_2)},\ b_b^{(e_2)} < 0 \tag{6}$$

Subscript b in (6) denotes the branch index in a bifurcation; we omit it in what follows as the process is the same for any branch.

We have extended our previous model [17], [24] to introduce more coupling between the four lines delineating the artery wall, and thus to better drive their evolution to the solution, even in case of textured background or local blur. Eq. (7) introduces the general formulation of our model, considering a reference line $V^{(R)}$ and three other curves $V^{(i)}$, $V^{(k)}$ and $V^{(l)}$, all three defined by their distance $b^{(i,k,l)}$ to $V^{(R)}$. The active contour is $V^{(i)}$ while $V^{(R)}$, $V^{(k)}$ and $V^{(l)}$ are known and fixed. The initial $V^{(i)}(s)$ is iteratively evolved in order to minimize the following energy functional:

$$E\left\{b^{(i)}|V^{(R)},b^{(k)},b^{(l)}\right\} = \int_0^1 P\left(V^{(R)}(s),b^{(i)}(s)\right) + \frac{\varphi}{2}\,b^{(i)'^2}(s) + \frac{\rho}{2}\left(b^{(i)}(s)-b^{(k)}(s)\right)^2 + \frac{\delta}{2}\left(b^{(i)'}(s)-b^{(l)'}(s)\right)^2 ds \tag{7}$$

The first term, $P(V^{(R)}(s), b^{(i)}(s))$, is the usual image potential at $V^{(i)}(s)$, defined as the gradient vector flow [38] to attract the curve $V^{(i)}(s)$ to the high gradients in the image and so reach contours. The other terms are regularization terms that express structural constraints, namely:

-$V^{(i)}(s)$ and $V^{(R)}(s)$ should be approximately parallel (which is expressed by the fact that the first derivative of the distance between them is minimized),
-$V^{(i)}(s)$ and $V^{(k)}(s)$ should be close to each other,
-$V^{(i)}(s)$ and $V^{(l)}(s)$ should be almost parallel.

The parameters φ, ρ and δ weight the relative influence of the structural constraints.

We rely on this model to extract the wall of each arterial branch ($V^{(i_1)}$, $V^{(i_2)}$, $V^{(e_1)}$, $V^{(e_2)}$) given the central reflection line $V^{(R)}$ (Fig. 5). For the segmentation of the lumen (i.e., inner contours i_1 and i_2, step C in Fig. 3), we exploit the symmetry of the interfaces with respect of the central reflection line and we minimize:

$$E\left\{b^{(i_1)}|V^{(R)},-b^{(i_2)},-b^{(i_2)}\right\} + E\left\{b^{(i_2)}|V^{(R)},-b^{(i1)},-b^{(i_1)}\right\} \tag{8}$$

Parameter $\rho > 0$ forces the symmetry with respect to the center line, while parameter $\delta > 0$ favors similar shape for the two opposite curves (Fig. 6(c)).

A similar process is then applied to extract the outer borders (e_1 and e_2, step D in Fig. 3), minimizing this time:

$$E\left\{b^{(e_1)}|V^{(R)},-b^{(e_2)},b^{(i_1)}\right\} + E\left\{b^{(e_2)}|V^{(R)},-b^{(e1)},b^{(i_2)}\right\} \tag{9}$$

This model imposes some symmetry of the external borders with respect to the central reflection line and a parallelism of the curves delineating the arterial wall (Fig. 6(d)). Note that the model (7) would allow us to impose a symmetry of the wall thickness with respect to $V^{(R)}(s)$ but it has not proved to be beneficial in the general case.

More implementation details are given in the Appendix, especially the initialization steps (both usage modes) and the parameterizations at each step. Briefly, the only difference between the automatic and semi-automatic modes is the initialization of the inner contours (steps A/A' and B/B' in Fig. 3), either from the binary mask output by the U-Net or from the central reflection line manually defined. In Fig. 6, we illustrate the semi-automatic case with the 3 central lines entered by the user (Fig. 6(a)), the inner borders being initialized based on grey-level and gradient criteria (Fig. 6(b)). For the parameterization, the following strategy proved very efficient for minimizing the energy functionals (8) or (9): at the beginning, φ, ρ, δ are set to large values to ensure robustness and then the constraints are relaxed for refinement.

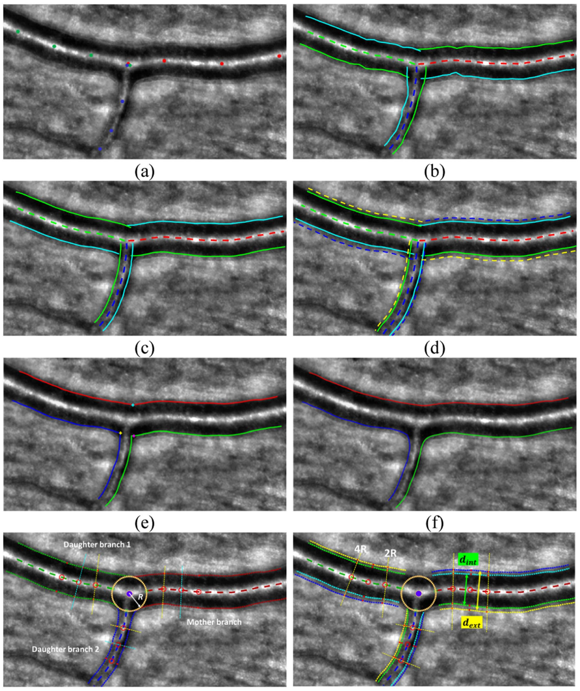
(a) (b) (c) (d) (e) (f) (g) (h)

Fig. 6. Segmentation at a bifurcation. (a) Manual initialization of the three central reflection lines (Fig. 3(A')); (b) inner contour initialization (B'); (c) final segmentation of the inner contours (C); (d) final segmentation of the artery wall for the three branches (D); (e) initialization of the three curves delineating the bifurcation, deduced from the branch segmentation; (f) final segmentation of the lumen at the arterial bifurcation (E); (g) inscribed circle and estimation of the branch diameters; (h) arterial wall segmentation and estimation of the inner and outer diameters.

3) *Active Contour Model for the Refinement at a Bifurcation:*

Since a precise segmentation at bifurcations is crucial to derive relevant measures, once each branch is segmented, their crossing at bifurcations can be analyzed and refined for a more accurate and more consistent bifurcation segmentation [18].

The method consists in detecting the intersection points between two contours and rearranging them to obtain three segmentation lines $C_i^{(0)}$, $i = 1, 2, 3$, as shown in Fig. 6(e). This new configuration is taken as the initialization of an active contour model, evolving to minimize:

$$E\{C_i\} = \int_0^1 P(C_i(s)) + \alpha(s)\left|C_i'(s)\right|^2 + \psi(s)\left|C_i'(s) - C_i^{(0)'}(s)\right|^2 ds \tag{10}$$

so as to refine the segmentation and ensure that the contours converge precisely to the inner wall of the vessels at the bifurcation without moving outside of this area, where the initial segmentation was precise. The algorithm is applied three times, on each line C_i independently of the other two. The energy functional (10) is derived from [34]. The last extra term imposes that the curve cannot move far away from its initial position. One main feature of the proposed method is that it adapts itself to the size and geometry of the vessel branches, without any tuning, which makes its use in concrete clinical applications very easy. Indeed, the model parameters, $\alpha(s)$ and $\psi(s)$, are calculated automatically along the curve according to local characteristics (vessel sizes and angles between branches). $\psi(s)$ takes low values near the bifurcation, to authorize the refinement, and higher values otherwise, to prevent C_i to move significantly along the branches. $\alpha(s)$ adjusts the strength of the first regularization term according to the geometry of the bifurcation (angle between branches) and the distance to the bifurcation. More details are given in [18].

4) Biomarker Estimation: The obtained segmentations enable us to calculate the biomarkers introduced in Section II-B. We estimate the branch diameters in regions derived from the largest circle inscribed in the bifurcation (i.e., tangent to the segmentation), similarly to [39] (Fig. 6(g) and (h)). Let us denote by R the radius of this circle. For the bifurcation biomarkers, the measurement region starts at a distance equal to one radius R from the intersection point between the circle and the central reflection, up to $2R$ (Fig. 6(g)). The mother branch is supposed to be the one with the highest diameter, but this decision can be manually corrected by the user who knows the direction of the blood flow. We calculate the median of the diameters measured in this region (more robust to outliers than the mean value). We also calculate the wall to lumen ratio (wlr) near the bifurcation, for the three branches. This time, we take a larger area $[R, 3R]$ and the wlr is the median value of all local measurements (Fig. 6(h)).

5) Supervision: The first level of possible supervision is at the initialization of the semi-automatic mode, where the user explicitly specifies which branches he want to process: as described previously, he has only to define the central reflection line of the three bifurcation branches by a few points, the rest of the segmentation being carried out automatically. Once the segmentation is completed, the user can check it visually and reinitialize the segmentation of any inner or outer contour that he is not satisfied with: he just defines a few points on the interface to reprocess, which are then interpolated, and the active contour model is re-applied with this new initialization. This is the second level of supervision, which can also be applied in the fully automatic mode. The flexibility in the usage modes of our software, its modularity as well as the simplicity of the optional manual interventions make AOV a very powerful tool for large-scale clinical studies.

IV. BIOMARKER SENSITIVITY TO SEGMENTATION IMPRECISION

Biomarkers are computed from diameter values derived from the image segmentation. So, segmentation imprecision results in errors in the estimation of biomarkers. We have studied mathematically and numerically the sensitivity of the junction exponent x (2), the deviation of the branching coefficient β_{dev} (5) and the wall to lumen ratio wlr (1) to an error of ε pixels in the estimate of diameters. The pixel size is $0.8\,\mu$m in our AOO images. Experiments were conducted on the sub-database *B* (268 bifurcations, Section II-C) for which we have reliable segmentations made with AOV under supervision. It covers the data variability in terms of vessel sizes ($d_0 \in [20,\ 130]$ μm, median: 76μm), and bifurcation asymmetry ($\lambda\epsilon[0.25,\ 1.00[$, median 0.62) and will be used to investigate the behavior of the biomarkers and validate our mathematical models.

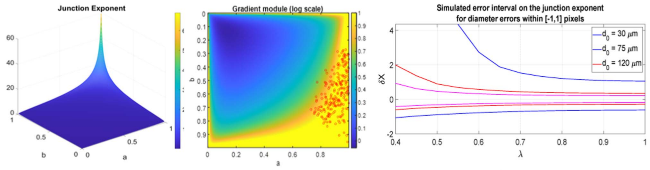

(a) (b) (c)

Fig. 7. Sensitivity of the junction exponent x to diameter estimation errors; (a) x as a function of the normalized diameters a and b, when $a < 1$; (b) slope of the function $x = R(a, b)$ in logarithm scale and after clipping at 10; red dots represent the normalized diameters found in our database; (c) interval of error in the estimation of x for an ideal bifurcation with $x = 3$, when errors within $[-1,\ 1]$ pixel are committed on the 3 diameters (with pixel size ~0.8 μm).

A. Junction Exponent

This bifurcation parameter is the value x solution of the equation $a^x + b^x - 1 = 0, (a, b) \in]0,\ 1[\times]0,\ 1[$, where $a = \frac{d_1}{d_0}, b = \frac{d_2}{d_0}$ are the daughter diameters normalized to the parent branch diameter (2). The graphical representation of x as a function $R(a, b)$ (Fig. 7(a)) shows that this biomarker is very sensitive to diameter imprecision, since the usual values of (a, b) are in a region of high slope (Fig. 7(b)).

In the following simulation, we consider an ideal bifurcation with $x = 3$ and we assume that errors $\varepsilon_i\epsilon[-1,\ 1]$ pixel are made simultaneously on the 3 diameters $d_i,\ i = 0,\ 1,\ 2$. Fig. 7(c) shows the resulting interval of error on x as a function of the asymmetry coefficient λ (4), for 3 different values of the mother branch diameter d_0 in AOO resolution. For an ideal bifurcation ($x = 3$) with median parameters $d_0 = 75\mu m,\ \lambda = 0.6$, the error interval is $[-0.38, +0.56]$, meaning that the measured value is in $[2.62,\ 3.56]$. As expected, the situation is even worse in standard retinography (pixel size $= \sim 10\mu$m), with a much larger error interval $[-1.8, +7.1]$. The error interval is greater for lower asymmetry coefficient λ, and other experiments show that it increases with x, which is consistent with the slope of $x = R(a, b)$ (Fig. 7(a) and (b)).

We conclude that the junction exponent exhibits poor properties: it is very sensitive to segmentation imprecision with intervals of errors that depend obviously on the size of the vessels (d_0), but also on the geometry of the bifurcation (λ) and the value to be measured (close to the optimum $x = 3$ or not).

B. Deviation of the Branching Coefficient $\beta_{\mathbf{dev}}$

As previously, we compute the biomarker β_{dev} (5) as a function of the normalized diameters a et b (Fig. 8). We notice that the slope of $\beta_{dev}(a, b)$ is much more constant than that of the junction exponent (see the isolines, which are regularly spaced over the domain of usual β_{dev} values). So, the estimation of errors will be much more stable and does not depend so strongly on the bifurcation geometry.

In contrast to the junction exponent, we can express analytically β_{dev} as a function of the three diameters (5). So, we can calculate the combined uncertainty in the measurement of β_{dev}, given the measured diameters d_0, d_1, d_2 and the uncertainty in

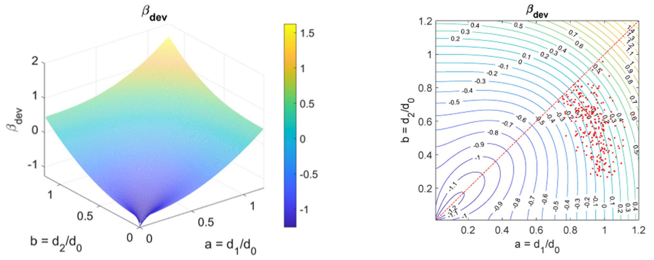

(a) (b)

Fig. 8. Graphical representation of β_{dev} as a function of the normalized diameters a and b (a) and isolines (b); the red dots: values in our database.

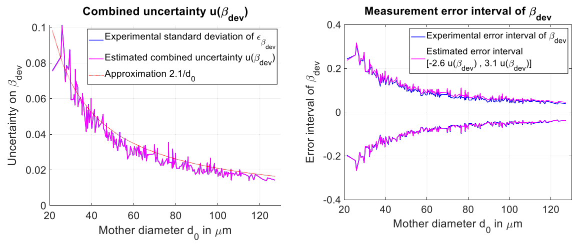

(a) (b)

Fig. 9. Sensitivity of β_{dev} to errors in diameter measurements. These results obtained on the 268 bifurcations of the database are presented by increasing values of the mother branch diameter. (a) Combined uncertainty $u(\beta_{dev})$ and (b) error interval of β_{dev}, for measurement errors ε_{d_i} on diameters d_i uniformly distributed in $[-1, +1]$.

each measurement. Let us denote by $u(d_i)$ the uncertainty in the measurement of d_i; it corresponds to the standard deviation of the distribution of d_i measurements, in pixels, or equivalently to the standard deviation of the distribution of measurement errors ε_{d_i} [40]:

$$u\left(d_i\right) = \sigma_{\varepsilon_{d_i}} = \sqrt{\left\langle \varepsilon_{d_i}^2 \right\rangle} \tag{11}$$

According to [40], the measurement error for β_{dev} can be approximated by:

$$\varepsilon_{\beta_{dev}} = \sum_{i=0}^{2} \left(\frac{\partial \beta_{dev}}{\partial d_i} \left(d_0, d_1, d_2\right) \right) \varepsilon_{d_i} \tag{12}$$

with $\beta_{dev}(d_0, d_1, d_2)$ defined by (5). We estimate the combined uncertainty $u(\beta_{dev})$ by calculating the standard deviation $\sigma_{\varepsilon_{\beta_{dev}}}$ of $\varepsilon_{\beta_{dev}}$. Assuming that the measurement errors ε_{d_0}, ε_{d_1}, ε_{d_2} are independent and that the uncertainty in the measurement of every diameter (11) is the same ($u(d_i) = \sigma_{\varepsilon_d}$), we get:

$$u\left(\beta_{dev}\right) = \sigma_{\varepsilon_d}\, u^{(1)}\left(\beta_{dev}\right) \tag{13}$$

$$\text{with} \quad u^{(1)}\left(\beta_{dev}\right) = \sqrt{\sum_{i=0}^{2} \left(\frac{\partial \beta_{dev}}{\partial d_i}(d_0, d_1, d_2) \right)^2}$$

$$\text{and} \quad \begin{cases} \frac{\partial \beta_{dev}}{\partial d_0}\left(d_0, d_1, d_2\right) = \frac{1}{d_0}\left[-2a^2(1+\lambda^2)\right] \\ \frac{\partial \beta_{dev}}{\partial d_1}\left(d_0, d_1, d_2\right) = \frac{1}{d_0}\left[2a + \frac{2}{a}\lambda^2 \frac{(1-\lambda)}{(1+\lambda^3)^{\frac{5}{3}}}\right] \\ \frac{\partial \beta_{dev}}{\partial d_2}\left(d_0, d_1, d_2\right) = \frac{1}{d_0}\left[2\lambda a - \frac{2}{a}\lambda \frac{(1-\lambda)}{(1+\lambda^3)^{\frac{5}{3}}}\right] \end{cases}$$

$u^{(1)}(\beta_{dev})$ is the combined uncertainty for error measurements in the diameters with a standard deviation of 1 pixel. For another distribution spread, we get the combined uncertainty $u(\beta_{dev})$ by just multiplying by the standard deviation σ_{ε_d}.

We relied on our sub-database *B* to validate this model and give an experimental estimate of the interval of error for any measurement of β_{dev}. We considered that the diameter values stored in the database are the exact diameter values, and we simulated measurement errors by adding errors ε_{d_i} following a uniform distribution in $[-1, +1]$ ($\sigma_{\varepsilon_d} = \sqrt{1/3}$). So, for each bifurcation, we got a set of experimental measurements of β_{dev} with measurement errors $\varepsilon_{\beta_{dev}}$. We compared the standard deviation $\sigma_{\varepsilon_{\beta_{dev}}}$ of these errors with the uncertainty given by (13). The root mean square error between both sets of values is equal to $4.5.10^{-5}$, validating our model (Fig. 9(a)).

For each bifurcation of the database, we also noted the negative $\varepsilon_{\beta_{dev}}^{\min}$ and positive $\varepsilon_{\beta_{dev}}^{\max}$ extrema of $\varepsilon_{\beta_{dev}}$ in order to delimit the error, $[\beta_{dev} + \varepsilon_{\beta_{dev}}^{\min},\ \beta_{dev} + \varepsilon_{\beta_{dev}}^{\max}]$ giving the smallest interval containing all experimental measurements. Then, we related the obtained intervals (Fig. 9(b), blue) to the combined uncertainty (13) by looking for the factors $k_{n,p}$ so that the estimated error intervals $[k_n u(\beta_{dev}), k_p u(\beta_{dev})]$ approximate at best the experimental intervals $[\varepsilon_{\beta_{dev}}^{\min}, \varepsilon_{\beta_{dev}}^{\max}]$ for all bifurcations. We sought these factors k_n and k_p experimentally, through a least square minimization over the 268 bifurcations of sub-database *B*. We found this approximation: $[-2.65\, u(\beta_{dev}), 3.14\, u(\beta_{dev})]$. The estimated error intervals fit then closely the experimental ones ($RMS \approx 3.10^{-3}$, Fig. 9(b), magenta).

This study gives us an idea about the accuracy we can expect in a measurement of β_{dev}. Given the measurements of the three diameters d_0, d_1, d_2 with a precision about $\pm\varepsilon$ pixels we can deduce that β_{dev} is obtained at about $\pm 3u(\beta_{dev})$. The shape of the error curves in Fig. 9(b) shows that bifurcations involving small arteries ($d_0 < 60\ \mu$m) are much more sensitive to diameter estimation errors than larger ones. In fact, the error on β_{dev} is essentially related to d_0: our experiments show that $u(\beta_{dev}) \approx \frac{2.1}{d_0}$ (Fig. 9(a), red dots), meaning that the sensitivity of this biomarker depends mainly on the size of the vessels and much less on the geometry of the bifurcation or its proximity to the theoretical optimality, which is in agreement with the slope of the function $\beta_{dev}(a, b)$ (Fig. 8). It is also worth noting the importance of image resolution: the same study in cSLO would lead to a combined uncertainty multiplied by a factor 10.

C. Wall to Lumen Ratio **Wrl**

Following a similar methodology as for β_{dev}, we first calculate from (1) the combined uncertainty, given the standard uncertainty σ_{ε_d} on diameters d_{int} and d_{ext}:

$$u\ (wlr) = \frac{\sigma_{\varepsilon_d}}{d_{int}} \sqrt{\left(\frac{d_{ext}}{d_{int}}\right)^2 + 1} \tag{14}$$

This formula shows that the uncertainty on the wall to lumen ratio is essentially of the order of $1/d_{int}$ since the ratio d_{ext}/d_{int} has a small variance (less than 0.2, experimentally verified). We also relied on our database to verify the validity of (14) (Fig. 10(a)) and to relate the uncertainty $u(wlr)$ to the error interval measured experimentally. For diameter errors ε_d

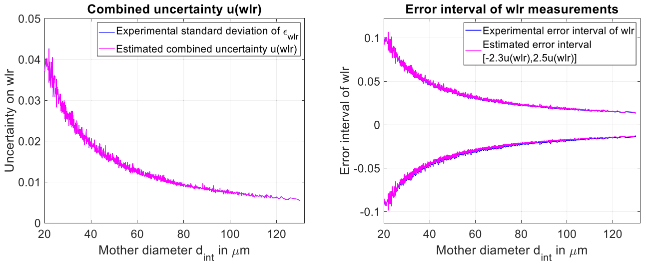

(a) (b)

Fig. 10. Sensitivity of wlr to errors in diameter measurements. (a) Combined uncertainty $u(wlr)$ and (b) error interval of wlr, for measurement errors ε_{d_i} on diameters d_{int}, d_{ext} uniformly distributed in [-1,+1].

uniformly distributed within $[-1,\ 1]$, we obtained the following error interval: $\varepsilon_{wlr} \in [-2.3u(wlr), 2.5u(wlr)]$ (Fig. 10(b)). In AOO images, the relative error for a normal small artery ($d_{int} = 20\ \mu$m, $wlr \approx 0.3$) is around $\pm 30\%$ while it is less than $\pm 10\%$ for normal arteries with $d_{int} \geq 70\ \mu$m. Again, the importance of the image resolution and the caliber of the artery is worth to be noted.

V. Evaluation of the Proposed Algorithms

We consider the two usage modes of AOV introduced in Section III-B (Fig. 3) with the segmentation methods described in Section III-C: (1) the fully automatic mode based on the active contour models initialized from the binary segmentation mask output by the U-Net; (2) the semi-automatic mode, where the central reflection line of the 3 bifurcation branches is initialized manually.

AOV was used in the semi-automatic mode under supervision to process the 268 images of sub-database B. It means that the medical experts checked the segmentations of the arterial branches and could reinitialize the active contour models until they were satisfied with the result. The refinement of the bifurcation segmentation is always done automatically, as well as the estimation of the diameters and biomarkers.

Thus, considering the semi-automatic mode under supervision, we first study the reproducibility of the segmentation and measurements with respect to image acquisition and to AOV users (Section V-A). Then, we evaluate the robustness and the accuracy of the automatic processing methods (Section V-B).

A. Evaluation of the Semi-Automatic Mode Under Supervision

We study here the reproducibility of the biomarker estimations in the semi-automatic mode under supervision. The issue is to evaluate the variability in the measurements resulting from a variability in the image acquisition or from variabilities in the supervised segmentation of a given image.

1) Reproducibility With Respect to Image Acquisition: Seven images of the same arterial bifurcation were acquired from a control subject, at 10 minutes interval. Two different experts segmented these images in the supervised mode. Table I presents the obtained measurements. The second daughter branch was too blurred to allow for wrl measurement. This experiment shows that the values do not undergo a significant change either between the different acquisitions or between the two experts: for each expert, the standard deviation of every measure is very low and the difference between experts is very small as well. This means that the biomarkers are robust to acquisition and that the estimates made under AOV from the supervised segmentations are reproducible, for the same user and among users.

TABLE I

Reproducibility With Respect to Image Acquisition

	d_0 (pix)	d_1 (pix)	d_2 (pix)	β_{dev}	x	wlr_0	wlr_1
Expert 1	107.48 $\pm$ 0.73	95.46 $\pm$ 1.52	72.18 $\pm$ 2.03	0.00 $\pm$ 0.03	3.02 $\pm$ 0.17	0.20 $\pm$ 0.01	0.19 $\pm$ 0.01
Expert 2	107.53 $\pm$ 0.76	95.38 $\pm$ 1.39	72.20 $\pm$ 2.16	0.00 $\pm$ 0.03	3.01 $\pm$ 0.19	0.20 $\pm$ 0.01	0.20 $\pm$ 0.01
Inter-experts	$\mathbf{-0.05}$ $\mathbf{\pm 0.12}$	$\mathbf{+0.07}$ $\mathbf{\pm 0.25}$	$\mathbf{-0.03}$ $\mathbf{\pm 0.25}$	$\mathbf{0.002}$ $\mathbf{\pm 0.005}$	$\mathbf{0.01}$ $\mathbf{\pm 0.03}$	$\mathbf{-0.005}$ $\mathbf{\pm 0.006}$	$\mathbf{-0.003}$ $\mathbf{\pm 0.011}$

TABLE II

Inter-Experts Analysis (34 Bifurcations)

Measure	**#**[a]	**Interval**[b] **(μm)**	**Mean, standard deviation**[b] **(μm)**	**Difference**[c] (pixels)
		Arterial bifurcation characterization		
d_0, d_1, d_2	86	[22.66 , 150.07]	63.91 +/- 29.47	**0.11 +/- 1.57**
x	20	[1.88 , 4.95]	3.23+/- 0.94	**-0.01 +/- 0.36**
β_{dev}	22	[-0.27 , 0.23]	0.02 +/- 0.13	**0.00 +/- 0.04**
		Arterial wall characterization		
d_{int}	55	[24.72 , 130.13]	63.49 +/- 27.25	**0.04 +/- 1.31**
d_{ext}	55	[38.92 , 152.44]	84.35 +/- 35.12	**0.21 +/- 2.70**
e	55	[4.31 , 24.57]	4.31 +/- 24.57	**0.32 +/- 1.68**
wlr	55	[0.14 ; 0.65]	0.34 +/- 0.10	**0.00 +/- 0.07**

[a] # indicates the number of measures; [b] the two columns show the statistical distribution of the measures; [c] this column indicates the mean and standard deviation of difference in the measures derived from the segmentation supervised by the two experts.

2) Reproducibility With Respect to Image Segmentation: We study here the variability in the estimation of biomarkers due to the use of AOV by different experts, still under supervision. 34 bifurcations, randomly selected from sub-database B, were processed by two different experts. We compare here the obtained measures characterizing the bifurcation (Fig. 6(g)) and the arterial wall (Fig. 6(h)). The inner diameters d_{int} are similar to $d_{i\ =\ 0,\ 1,\ 2}$ but estimated on a larger area; the wall thickness is defined by $e\ = \frac{d_{ext} - d_{int}}{2}$. For the analysis of the differences, we only take the measures deemed possible (that is, the image quality is sufficient) by the two users simultaneously. Thus, out of the 102 segmented branches, both experts agreed that 86 of them have internal contours that can be segmented everywhere, thus leading to reliable measurements of diameters $d_0,\ d_1$ or d_2. They had the same appreciation (can be segmented / cannot be segmented) in 84% of cases. Out of the 34 bifurcations analyzed, the two experts judged that 22 of them have all three branches that can be segmented, thus leading to reliable measurements of bifurcation parameters x and β_{dev} (two junction exponents had meaningless negative values ($a > 1$)). Both experts agreed that they can segment the inner and outer borders on both sides for 55 branches out of the 102, thus leading to wlr estimates.

Table II summarizes the results. The statistics regarding each parameter demonstrate that the sub-database used in this experiment covers the variability of arterial bifurcations. The proportion of rejected measurements, because of the poor quality of

TABLE III
STATISTICS ABOUT THE MEASUREMENTS DEDUCED FROM THE SUPERVISED SEGMENTATIONS MADE BY THE EXPERT (141 BIFURCATIONS)

d_0 [a]	d_1 [a]	d_2 [a]	λ
97.46 ± 26.95	89.34 ± 25.02	55.47 ± 20.37	0.62 ± 0.19

x	β_{dev}	wlr_0	wlr_1	wlr_2
3.86 ± 2.34	0.00 ± 0.13	0.29 ± 0.07	0.29 ± 0.07	0.37 ± 0.08

[a] Diameters are expressed in pixels (pixel size $\cong 0.8\mu m$)

TABLE IV
EVALUATION OF THE SEGMENTATION PROVIDED BY THE U-NET AT THE BIFURCATION (110 IMAGES)

Recall	Precision	Dice
0.97 ± 0.02	0.98 ± 0.03	0.98 ± 0.02

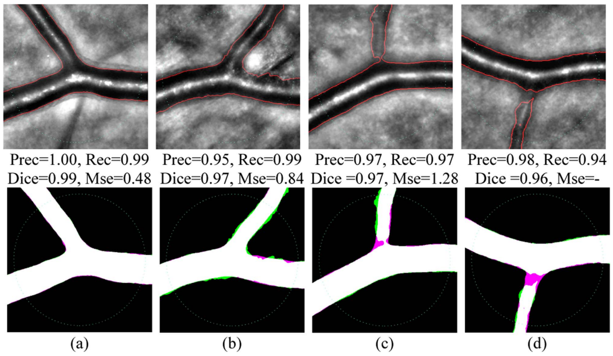

(a) (b) (c) (d)

Fig. 11. Examples of binary masks with metrics. (Precision (Prec), Recall (Rec) Dice score (Dice) and Root mean square error (mse)). The dashed circle indicates the area of evaluation. First row: boundaries of the binary mask superimposed on the source image. Second row: binary mask with in white the true positives, in green the false positives and in magenta the false negatives.

the source image in the concerned zone, shows that blur of some interfaces is the main limitation: difficulty to obtain reliable measurements and potential disagreement regarding keeping or rejecting the measure. But we observe a very good agreement for the measurements kept by both experts: for inner diameters ($d_{0,\,1,\,2},\ d_{int}$), the mean bias is very low and the standard deviation is around 1.5 pixels. This leads to small differences in the estimation of β_{dev} and even x. The difference for the outer diameter is greater, which was expected given that the outer interface is much less contrasted and much more ambiguous. However, the agreement on the wlr is very good without bias ($0.00 +/- 0.07$).

B. Evaluation of the Semi-Automatic and Automatic Modes Without Expert Supervision on Segmentation Results

We have just demonstrated the inter-expert reproducibility of the measurements in the supervised mode. We can now evaluate our processing methods by comparing the results obtained in the automatic and semi-automatic modes with those provided by an expert in the supervised mode.

1) Sub-Database: We extracted from sub-database B the 141 images whose quality was deemed satisfactory; that is, all images that met the following criteria: the 3 branches have a diameter greater than 30μm, none of them has a blurred wall on both sides simultaneously; veins can cross arterial branches, but not at the bifurcation (too complex topology to be recovered from the binary mask). These 141 images cover the full variability of arterial bifurcations (Table III) and will serve as ground truth in this evaluation.

2) Binary Segmentation With the U-Net and Evaluation: We applied our U-Net on the sub-database of 141 images. The visual inspection of the results shows that our model can extract the vascular tree, including simple arteries, simple veins, simple bifurcations and arteriovenous crossings (Fig. 4). The automatic segmentation provided by the neural network was evaluated by comparing the predicted segmentation mask and the reference segmentation using standard indices: recall, precision and Dice scores. In this study, we consider only a region of interest centered on the bifurcation: a disk of radius $4R$ where R is the radius of the circle inscribed in the bifurcation. We excluded 31 images for which a vein crosses this region (not segmented in the ground truth).

Table IV summarizes the results obtained on the 110 considered bifurcations. All metrics are very close to 1, with low standard deviations, demonstrating the accuracy and the robustness of the proposed method. The binary mask is especially good for well contrasted images (Fig. 11(a)), less accurate and more indented for more blurred cases (Fig. 11(b)). However, the detection of small branches is not always precise, especially at the branching (Fig. 11(c)), and sometimes not consistent (Fig. 11(d)). This happens when the black area between the central reflection and the vessel lumen becomes gray because the small vessel is not planar enough in the eye fundus. Thus, the vessel will be classified partially as background. On the complete database of 141 images, we obtained 128 masks (91%) with a complete detection of the bifurcation against 13 with a partial one.

3) Evaluation of the Automatic Processing of Arterial Bifurcations: The automatic processing of bifurcations results from the binary segmentation made by the U-Net followed by the refinement with the active contour models (Section III-C, Appendix). We first evaluate the accuracy of the fully automatic segmentation by computing the mean square error between the reference contours and the automatic segmentations, before and after applying the deformable models. Again, this is achieved on the region of interest centered on the bifurcation (Section V-B-2). We also evaluate the accuracy in the estimation of diameters and biomarkers. The values are estimated on 118 images of the sub-database, for which the complete processing (U-Net and deformable models) was successful (consistent binary mask and bifurcation structure well recovered). The statistics concerning the U-Net images (without refinement) relate to 110 bifurcations (as in Section V-B-2): 8 bifurcations have an arteriovenous crossing over a diameter estimation zone, not allowing us to estimate the diameter for the three branches (unlike the deformable models which allow for an extrapolation). Results are presented in Table V, first and second lines.

After the refinement step with the proposed parallel deformable models, the mean square error between the reference contours and the automatic segmentations is reduced from 3.00

TABLE V

EVALUATION OF THE ESTIMATION OF DIAMETERS AND BIFURCATION BIOMARKERS (118 OR 110 IMAGES)

	$\boldsymbol{\delta d_0}$ [a]	$\boldsymbol{\delta d_1}$ [a]	$\boldsymbol{\delta d_2}$ [a]
U-Net [b]	-1.43 ± 3.26	-0.68 ± 2.93	1.71 ± 4.73
Automatic mode [c]	-0.30 ± 1.98	$\mathbf{-0.20 \pm 2.25}$	$\mathbf{1.07 \pm 3.97}$
Semi-auto. Mode [d]	$\mathbf{-0.15 \pm 2.10}$	0.22 ± 2.76	2.71 ± 7.20
	$\boldsymbol{mse}$ [a]	$\boldsymbol{\delta \beta_{dev}}$	$\boldsymbol{\delta x}$
U-Net [b]	3.00 ± 2.30	0.06 ± 0.13	1.13 ± 2.46
Automatic mode [c]	$\mathbf{1.75 \pm 1.24}$	$\mathbf{0.01 \pm 0.08}$	$\mathbf{-0.13 \pm 2.11}$
Semi-auto. Mode [d]	1.87 ± 1.85	0.03 ± 0.12	-0.15 ± 2.25

[a] Expressed in pixels (pixel size $\cong 0.8\mu m$). [b] Estimated from the boundaries of the binary mask at the output of the U-Net. [c] After applying the deformable models (which gives the evaluation of the fully automatic mode against the segmentations made under supervision). [d] In the semi-automatic mode where the central reflection lines are initialized by the user, without any supervision on the segmentation results.

TABLE VI

EVALUATION OF THE ESTIMATION OF THE WALL TO LUMEN RATIO FOR THE 3 BRANCHES INVOLVED IN A BIFURCATION (118 OR 110 IMAGES)

	δwlr_0	δwlr_1	δwlr_2	$\delta wlr_{0,1,2}$
Automatic mode (110 images)	0.004 ± 0.059	0.007 ± 0.080	-0.014 ± 0.112	-0.001 ± 0.086
Semi-auto. Mode (118 images)	0.004 ± 0.052	0.005 ± 0.079	-0.020 ± 0.126	-0.004 ± 0.091

(+/− 2.30) pixels for the neural network prediction alone to 1.75 (+/− 1.24) pixels after the refinement step, which is a significant gain. Diameters are also much better estimated at the end of the process (mean error reduced by more than one pixel for the largest branches), justifying the effort to provide segmentations as accurate as possible. But, standard deviations range from 2 to 4 pixels, with, on average, an overestimation for the second daughter branch. Indeed, the smallest branches are often more blurred with an external border very close to the inner one. Considering all branches together, the error is equal to 0.19 +/− 2.92 while it was 0.11 +/− 1.57 when evaluating the inter-expert variability in the semi-automatic mode under supervision (Table II). The last two columns in Table V concern the errors committed on x and β_dev. Again, we can see the positive impact of improving segmentation accuracy, which is consistent with our study in Section IV. There is no significant bias, but the standard deviations remain too high with respect to the required accuracy. This is not surprising since very accurate values for all three diameters are required to achieve a good estimate of those biomarkers (Section IV-A, B). So, the expert remains mandatory to check the automatic segmentation and, if needed, refine it thanks to the possible reinitialization of the active contour models. However, it is worth noting that accurate diameters can now be obtained without any supervision for most branches: 70.3% of the 354 tested branches have an error less than 1 pixel, so that the proposed processing flow alleviates dramatically the expert's task. The difficulties remain at the level of the smallest branches, in case of blur.

We now introduce the segmentation of the outer border of the arterial wall of the three branches at a bifurcation and the wall to lumen ratio (Fig. 6(h)). The wlr is calculated in a region situated between $2R$ and $4R$ as the median value of all local wlr. Table VI shows the results (first line): the estimates are very accurate given the usual values of the wlr (around 0.3, Table III), which confirms that the wlr is a robust biomarker.

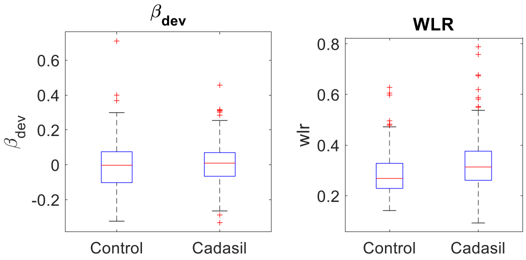

Fig. 12. Box plot of the biomarker measurements obtained with AOV.

4) Evaluation of the Semi-Automatic Processing of Arterial Bifurcations: In this mode, the user initializes the central reflection lines of the three branches, and the rest of the segmentation is fully automatic, as described in Section III-C and Appendix. The results are presented in Tables V and VI (last line). The segmentation is more accurate in the fully-automatic mode, with a mse equal to 1.75 pixels against 1.87, and with also a lower standard deviation. The diameter estimations of the biggest and well contrasted branches are slightly better in the semi-automatic mode, but significantly less good for the smaller ones. This again shows the ability of the U-Net to handle small and low contrast vessels. At the end, the bifurcation biomarkers are better evaluated in the fully automatic mode. Concerning the wall to lumen ratio, the results are slightly better for the fully automatic mode, but again, the most contrasted walls are better processed in the semi-automatic mode.

VI. MEDICAL APPLICATION

Medical experts of the Quinze-Vingts and Lariboisiere hospitals have processed hundreds images of control and CADASIL cases (Section II-C) with AOV used in the semi-automatic mode under supervision. The purpose is to statistically compare the two populations (no individual diagnosis is envisaged given the conclusions of our study in Section IV). The quality of the image at each segmented interface was annotated by the expert (correct vs. insufficient) in order to only compute relevant biomarkers. We restricted the analysis to the bifurcations with $d_2 > 30\mu$m. According to Section V-A-2) and Section IV-B, C, we can estimate that the standard uncertainty of diameters is around 1.5 pixel, the combined uncertainty for β_{dev} around 0.06 and the combined uncertainty for wlr around 0.031. Fig. 12 shows the distribution of the measurements for the two populations.

We did not find a statistically significant difference between healthy subjects and CADASIL patients for β_{dev} (0.006 ± 0.168 versus 0.005 ± 0.121). A two-sample t-test does not reject the null-hypothesis that the two samples come from normal distributions with equal means (p-value $= 0.96$ at the 5% significance level). By contrast, we found that CADASIL subjects exhibit in average an increased wlr: $wlr = 0.327 \pm 0.090$ against 0.284 ± 0.078 (p-value$< 10^{-3}$). A more in-depth clinical study was carried out by our medical partners and their results published in [41] are fully consistent with Fig. 12.

VII. CONCLUSION

We have presented a complete framework (AOV) for the segmentation of retinal vessels in AOO images and the computation of derived biomarkers characterizing an arterial network. Our approach relies on an optimized U-Net architecture to retrieve the vascular network and new active contour models to refine the lumen contour and segment the arterial walls. This combination takes advantage of both segmentation approaches: the ability of a CNN to learn the wide variability of images and vascular topologies, and the ability of deformable models to explicitly integrate prior knowledge (here approximate parallelism, symmetry properties) and reach high accuracy when well initialized. Our experiments demonstrate that our software tool provides reliable and accurate segmentations and measurements, with high reproducibility with respect to image acquisition and users. In the supervised mode, the average error on diameter estimates is around 0.11 +/− 1.57 pixel (0.09 +/− $1.2\mu m$), and the resulting β_{dev} and wlr are without bias. The fully automatic mode leads to good segmentations ($mse = 1.75 \pm 1.24$ pixel), with an overall error of 0.19 +/− 2.92 pixel in the diameter estimation, close to the inter-expert variability.

To our knowledge, AOV is the only framework that allows large-scale analysis of AOO images, with good accuracy and acceptable user involvement. Biomarkers are provided with the corresponding interval of error, which is another important contribution. In a preliminary clinical study, we found that the CADASIL population has statistically an increased wlr with respect of the control population (causes to be further explored).

We will now focus on the automatic recovery of the vascular network, to better handle arterio-venous crossing and classify vessels into veins or arteries. All these tools will pave the way for AOO image montage processing to address the whole vascular tree in both wide-field and high-resolution imaging, offering new avenues for medical diagnosis and clinical studies.

APPENDIX
IMPLEMENTATION DETAILS

We now detail how the active contour models are initialized in both usage modes and how the parameterization has been optimized. We review the stages A to D in Fig. 3.

A. Initialization of the Segmentation Process (Step A/A')

In the fully automatic mode, we first apply the U-Net to compute the binary mask whose borders match approximately the inner contour of the vessels (veins and arteries).

In the semi-automatic mode, the user sequentially defines the three branches involved in the bifurcation by clicking for each on a few points on its central reflection line.

B. Initialization of the Inner Contours (Step B/B')

The segmentation of the internal contours of each branch $b\epsilon\{0,\ 1,\ 2\}$ requires computing, at each position s, the distances $b_b^{i_k}(s),\ k = 1,\ 2$ to the reference line $V_b^{(R)}$ (6).

In the fully automatic mode, we first need to recover the vascular tree structure (i.e., $V_b^{(R)}$). This is achieved from the morphological skeleton of the binary mask (Fig. 13(a)). The branching points are analyzed to recover the main branches and the vascular structure (bifurcations and arteriovenous crossings). A classical active contour [34] is applied on the top-hat image to refine the position of each line toward the central reflection (Fig. 13(b)). Then, the distances $b_b^{(i_1,\ 2)}(s)$ to $V_b^{(R)}(s)$ are initialized from the boundaries of the binary mask, based on a minimal distance criterion (Fig. 13(c)).

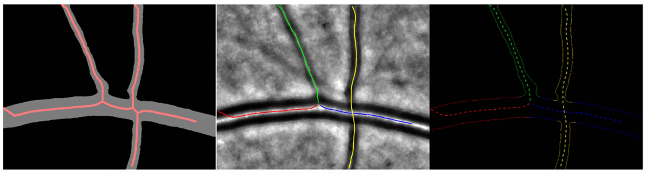
(a) (b) (c)

Fig. 13. Main steps to recover the vascular tree from the binary mask and initialize the active contour models. (a) Binary mask output by the U-Net (grey) and corresponding skeleton (red); (b) skeleton after analysis of the branching points and refinement based on the application of a classical snake [34]; (c) initialization of the active contour model.

In the semi-automatic mode, we initialize each central reflection line $V_b^{(R)}$ from the points entered by the expert and we also refine it on the top-hat image. Then, we estimate the local distances $b_b^{(i_1,\ 2)}(s)$ by optimizing local criteria on a window (of size 80μm) sliding along the central reflection (Fig. 6(b)). At each position, we test several radii, each one defining two segments delimiting the lumen on either side of $V_b^{(R)}$, and we retain the radius that minimizes the mean gray level between both segments. Finally, we refine this first estimate by maximizing the mean gradient module calculated on both segments.

C. Segmentation of the Inner Contours (Lumen, Step C)

We will omit subscript b in what follows as the process is the same for all three branches. We first apply the active contour model (7) (Section III-C-2) without the two last regularizations, considering only the approximate parallelism with respect to the central reflection line $V^{(R)}$. So, the contours are first evolved in order to minimize $E\{\ b^{(i_k)}|V^{(R)}, -, -\}$, on both sides $k = 1,\ 2$ independently, with $\varphi = 1000$, for a maximum of 5 iterations, which leads to a refined and smoother contour in comparison to the initialization (Fig. 6(b)). Then, the parallelism constraint with respect to $V^{(R)}$ is relaxed ($\varphi = 150$) for further very local refinement, and coupling is introduced by minimizing (8) (Fig. 6(c)). Experimentally, the following strategy proved very efficient: at the beginning, $\rho,\ \delta$ are set to large values to ensure robustness ($\rho = 0.1,\ \delta = 1000$), and then the constraints are relaxed for refinement with values $\rho = 0.1,\ \delta = 500$, then $\rho = 0.1,\ \delta = 0$, and finally $\rho = 0,\ \delta = 0$. Each step is iterated until a steady solution is obtained.

D. Segmentation of External Contours (Vessel Wall, Step D)

We initialize the external curves locally on a sliding window, by maximization of the mean local gradient module, given the inner borders. Then, the contours are evolved in order to minimize $\{\ b^{(e_k)}|V^{(R)}, -, -\},\ k = 1,\ 2$, with $\varphi = 1000$, for a maximum of 10 iterations. Again, a refinement is obtained by relaxing the parallelism constraint with respect to $V^{(R)}$, introducing coupling, and minimizing (9).

REFERENCES

[1] E. Koch et al., "Morphometric analysis of small arteries in the human retina using adaptive optics imaging: Relationship with blood pressure and focal vascular changes," *J. Hypertension*, vol. 32, no. 4, 2014, Art. no. 890.

[2] L. Arnould et al., "Using artificial intelligence to analyse the retinal vascular network: The future of cardiovascular risk assessment based on oculomics? A narrative review," *Ophthalmol. Ther.*, vol. 12, no. 2, pp. 657–674, Apr. 2023.

[3] T. Luo et al., "Retinal vascular branching in healthy and diabetic subjects," *Invest. Ophthalmol. Vis. Sci.*, vol. 58, no. 5, pp. 2685–2694, 2017.

[4] G. Leontidis, B. Al-Diri, and A. Hunter, "Summarising the retinal vascular calibres in healthy, diabetic and diabetic retinopathy eyes," *Comput. Biol. Med.*, vol. 72, pp. 65–74, 2016.

[5] N. Witt et al., "Abnormalities of retinal microvascular structure and risk of mortality from ischemic heart disease and stroke," *Hypertension*, vol. 47, no. 5, pp. 975–981, 2006.

[6] T. Y. Chui, T. J. Gast, and S. A. Burns, "Imaging of vascular wall fine structure in the human retina using adaptive optics scanning laser ophthalmoscopy," *Invest. Ophthalmol. Vis. Sci.*, vol. 54, no. 10, pp. 7115–7124, 2013.

[7] E. Bakker et al., "Adaptive optics ophthalmoscopy: A systematic review of vascular biomarkers," *Surv. Ophthalmol.*, vol. 67, pp. 369–387, Mar./Apr. 2022.

[8] T. F. Sherman, "On connecting large vessels to small: The meaning of Murray's law," *J. Gen. Physiol.*, vol. 78, no. 4, pp. 431–453, 1981, doi: 10.1085/jgp.78.4.431.

[9] S. Arichika et al., "Comparison of retinal vessel measurements using adaptive optics scanning laser ophthalmoscopy and optical coherence tomography," *Japanese J. Ophthalmol.*, vol. 60, no. 3, pp. 166–171, 2016.

[10] N. Chapman et al., "Computer algorithms for the automated measurement of retinal arteriolar diameters," *Brit. J. Ophthalmol.*, vol. 85, no. 1, pp. 74–79, 2001.

[11] S. Arichika et al., "Effects of age and blood pressure on the retinal arterial wall, analyzed using adaptive optics scanning laser ophthalmoscopy," *Sci. Rep.*, vol. 5, no. 1, 2015, Art. no. 12283.

[12] J. Hugo et al., "Morphologic analysis of peripapillary retinal arteriole using adaptive optics in primary open-angle glaucoma," *J. Glaucoma*, vol. 29, no. 4, pp. 271–275, 2020.

[13] R. A. Mehta et al., "Morphometric analysis of retinal arterioles in control and hypertensive population using adaptive optics imaging," *Indian J. Ophthalmol.*, vol. 67, no. 10, 2019, Art. no. 1673.

[14] A. Gallo et al., "Non-invasive evaluation of retinal vascular remodeling and hypertrophy in humans: Intricate effect of ageing, blood pressure and glycaemia," *Clin. Res. Cardiol.*, vol. 110, pp. 959–970, 2021.

[15] [Online]. Available: https://www.imagine-eyes.com/products/aodetect/#walls

[16] Imagine Eye rtx1, [Online]. Available: https://www.imagine-eyes.com/products/rtx1/

[17] N. Lermé et al., "A fully automatic method for segmenting retinal artery walls in adaptive optics images," *Pattern Recognit. Lett.*, vol. 72, pp. 72–81, 2016.

[18] I. Trimeche et al., "Segmentation of retinal arterial bifurcations in 2D adaptive optics ophthalmoscopy images," in *Proc. IEEE Int. Conf. Image Process.*, 2019, pp. 1490–1494.

[19] I. Trimeche et al., "Fully automatic CNN-based segmentation of retinal bifurcations in 2D adaptive optics ophthalmoscopy images," in *Proc. IEEE Int. Conf. Image Process. Theory, Tools Appl.*, 2020, pp. 1–6.

[20] C. D. Murray, "The physiological principle of minimum work: I. The vascular system and the cost of blood volume," *Proc. Nat. Acad. Sci. United States Amer.*, vol. 12, no. 3, pp. 207–214, 1926, doi: 10.1073/pnas.12.3.207.

[21] H. Chabriat et al., "CADASIL: Yesterday, today, tomorrow," *Eur. J. Neurol.*, vol. 27, no. 8, pp. 1588–1595, Aug. 2020.

[22] D. Lesage et al., "A review of 3D vessel lumen segmentation techniques: Models, features and extraction schemes," *Med. Image Anal.*, vol. 13, pp. 819–845, 2009.

[23] S. Moccia et al., "Blood vessel segmentation algorithms–review of methods, datasets and evaluation metrics," *Comput. Methods Programs Biomed.*, vol. 158, pp. 71–91, 2018.

[24] F. Rossant et al., "Parallel double snakes. Application to the segmentation of retinal layers in 2D-OCT for pathological subjects," *Pattern Recognit.*, vol. 48, pp. 3857–3870, 2015.

[25] O. Ronneberger, P. Fischer, and T. Brox, "U-Net: Convolutional networks for biomedical image segmentation," in *Medical Image Computing and Computer-Assisted Intervention*. Berlin, Germany: Springer, 2015, pp. 234–241.

[26] F. Isensee et al., "nnU-Net: A self-configuring method for deep learning-based biomedical image segmentation," *Nature Methods*, vol. 18, no. 2, pp. 203–211, 2021.

[27] G. Lepetit-Aimon, R. Duval, and F. Cheriet, "Large receptive field fully convolutional network for semantic segmentation of retinal vasculature in fundus images," in *Proc. 1st Int. Workshop, COMPAY 5th Int. Workshop*, 2018, pp. 201–209.

[28] P. Liskowski and K. Krawiec, "Segmenting retinal blood bessels with deep neural networks," *IEEE Trans. Med. Imag.*, vol. 35, no. 11, pp. 2369–2380, Nov. 2016.

[29] H. Fu et al., "DeepVessel: Retinal vessel segmentation via deep learning and conditional random field," in *Proc. Int. Conf. Med. Image Comput. Comput.-Assist. Interv.*, 2016, pp. 132–139.

[30] A. Lahiri et al., "Generative adversarial learning for reducing manual annotation in semantic segmentation on large scale miscroscopy images," in *Proc. IEEE Conf. Comput. Vis. Pattern Recognit. Workshops*, 2017, pp. 794–800.

[31] D. Li et al., "Residual U-Net for retinal vessel segmentation," in *Proc. IEEE Int. Conf. Image Process.*, 2019, pp. 1425–1429.

[32] K. He et al., "Deep residual learning for image recognition," in *Proc. IEEE Conf. Comput. Vis. Pattern Recognit.*, 2016, pp. 770–778.

[33] K. K. Maninis et al., "Deep retinal image understanding," in *Proc. Int. Conf. Med. Image Comput. Comput.-Assist. Interv.*, 2016, pp. 140–148.

[34] M. Kass, A. Witkin, and D. Terzopoulos, "Snakes: Active contour models," *Int. J. Comput. Vis.*, vol. 1, no. 4, pp. 321–331, 1988.

[35] C. Szegedy et al., "Inception-v4, inception-resnet and the impact of residual connections on learning," in *Proc. 31st AAAI Conf. Artif. Intell.*, 2017, pp. 4278–4284.

[36] J. Deng et al., "ImageNet: A large-scale hierarchical image database," in *Proc. IEEE Conf. Comput. Vis. Pattern Recognit.*, 2009, pp. 248–255.

[37] D. P. Kingma and J. Ba, "Adam: A method for stochastic optimization," in *Proc. Int. Conf. Learn. Representations*, 2015.

[38] C. Xu and J. L. Prince, "Snakes, shapes, and gradient vector flow," *IEEE Trans. Image Process.*, vol. 7, no. 3, pp. 359–369, Mar. 1998.

[39] S. Ramcharitar et al., "A novel dedicated quantitative coronary analysis methodology for bifurcation lesions," *EuroIntervention: J. EuroPCR Collaboration Work. Group Interventional Cardiol. Eur. Soc. Cardiol.*, vol. 3, no. 5, pp. 553–557, 2008.

[40] H. Castrup, "Estimating and combining uncertainties," in *Proc. 8th Annu. ITEA Instrum. Workshop*, 2004.

[41] M. Paques et al., "Early remodeling and loss of light-induced dilation of retinal small arteries in CADASIL," *J. Cereb. Blood Flow Metab.*, vol. 13, 2024, Art. no. 0271678X241226484.